ORIGINAL RESEARCH ARTICLE

Effect of Solidification Segregation on Microstructure and Mechanical Properties of a Ni-Cr-Mo-V Steel Weld Metal

CHAOYU HAN, QU LIU, ZHIPENG CAI, XIN HUO, MANJIE FAN, KEJIAN LI, and JILUAN PAN

The effects of solute elements segregation during solidification on microstructure evolution and mechanical properties of a Ni-Cr-Mo-V rotor weld metal were studied. The alloy elements, such as Mn and Ni, segregated at inter-dendritic (ID) region, resulting in microstructural inhomogeneity between ID and dendritic core (DC) region. The microstructure of ID and DC region was characterized in detail by transmission electron microscopy (TEM) and transmission electron backscatter diffraction (T-EBSD). The results showed that the microstructure of ID region was composed of untempered martensite and retained austenite, while the bainite and ferrite were found at DC region. Two morphologies of retained austenite, film-like and blocky, were formed at different nucleation sites within ID region. The film-like retained austenite distributed at low-angle martensite lath boundaries held a near Nishiyama–Wasserman (N–W) orientation relationship with its surrounding untempered martensite lath, while the blocky retained austenite distributed at high-angle boundaries held no special orientation relationship with surrounding matrix. The segregation behavior of alloy elements was analyzed by Scheil solidification simulation. The formation mechanism of untempered martensite and retained austenite was proposed and the effects of ID segregation on impact toughness and hardness were discussed.

https://doi.org/10.1007/s11661-022-06600-w

I. INTRODUCTION

WITH the trend of large-scaled development of steam turbines in the new fossil and nuclear power plants, it is very difficult to obtain large-sized rotors by forging.[1] Welding, as an effective joining method, is widely used to manufacture large turbine rotors.[2] In order to obtain a good combination of strength and toughness, various alloying elements are added to the welding consumables to optimize microstructure of weld metal.[3] Over the past few decades, the mixture microstructure of martensite and bainite has been considered to be a combination of well-balanced strength and toughness.[4] In addition to adjusting the microstructure of weld metal by compositions, welding methods and parameters are also important factors affecting the microstructure of weld metal.[5,6]

Multi-layer and multi-pass welding technique has been widely used in components with thick walls, such as steam turbine rotors,[7] and the microstructure of weld metal deposited by this technique exhibits heterogeneous feature due to the complex thermal cycling.[8] This heterogeneous feature of microstructure can be classified into two kinds of heterogeneity, i.e., macroscopic and microscopic microstructure heterogeneity.[9] From macroscopic perspective, the deposited weld metal is reheated by subsequent passes, and a part of the prior columnar grains is transformed into equiaxed ones.[10] From microscopic perspective, the solidification of weld metal usually takes place in the characteristic growth pattern of cellular dendritic, which leads to segregation of alloying and impurity elements to inter-dendritic (ID)

CHAOYU HAN, QU LIU, and JILUAN PAN are with the Department of Mechanical Engineering, Tsinghua University, Beijing 100084, P.R. China and also with the Key Laboratory for Advanced Materials Processing Technology, Ministry of Education, Beijing 100084, P.R. China. ZHIPENG CAI is with the Department of Mechanical Engineering, Tsinghua University and with the Key Laboratory for Advanced Materials Processing Technology, Ministry of Education and with the State Key Laboratory of Tribology, Tsinghua University, Beijing 100084, China and also with the Collaborative Innovation Center of Advanced Nuclear Energy Technology, Tsinghua University, Beijing 100084, China. XIN HUO and MANJIE FAN are with the Shanghai Electric Power Generation Equipment Co., Ltd., Shanghai, P.R. China. KEJIAN LI is with the Department of Mechanical Engineering, Tsinghua University and with the Key Laboratory for Advanced Materials Processing Technology, Ministry of Education and also with the State Key Laboratory of Advanced Welding and Joining, Harbin Institute of Technology, Harbin 150006, China. Contact e-mail: kejianli@mail.tsinghua.edu.cn
Manuscript submitted August 8, 2021; accepted January 9, 2022.
Article published online January 28, 2022

regions.[11] The heterogeneous distribution of alloying elements due to inter-dendritic segregation behavior will result in the difference of microstructure distributed at columnar grain zone during further cooling,[9] affect the size of the initial columnar grain size,[12,13] and influence the precipitation and distribution of carbides.[14,15] During solidification process, the diffusion direction of alloying element depends on the element equilibrium distribution coefficient k_{ele} in multicomponent system at the solid-liquid interface. During solidification process, when the value of k_{ele} is less than 1, the content of alloying element in the liquid is higher than that in the solid phase at the liquid–solid interface, resulting in higher content of alloying element in the subsequently formed solid phase than that in the previously formed solid phase. Consequently, element segregation develops most pronounced in the last solidified region, forming ID region.[16] Dupont et al[17] reported that Mo and Cr were enriched at ID regions, while Fe and Ni were depleted in a Fe-Ni-Cr-Mo alloy, and the segregation of alloy elements was not significantly affected by the cooling rates via comparing the results of differential thermal analysis (DTA) with a cooling rate of 5 °C/s and that of welded specimens. Powell et al.[18] found that the growth of δ-ferrite from the liquid phase is accompanied by elemental segregation behavior, and the increase of Mn and Ni contents rendered the ID regions more resistant to etching, appearing white in the light micrograph. They also found that the microhardness at the dendrite core (DC) regions was lower than that at the ID regions, but the microstructure at the ID regions was not analyzed in their work. Keehan et al[19–21] studied the effect of Ni content on microstructure of high strength steel weld metals. They found the significant segregation of Ni and Mn at ID regions and indicated that a mainly martensitic microstructure developed at ID regions, whereas bainite was found at DC regions. Keehan's work suggested that higher contents of alloying elements at ID regions stabilized austenite and led to a lower transformation temperature, resulting in microstructural inhomogeneity. This work firstly defined the microstructure type at ID and DC regions and gave a reasonable explanation; however, the effect of ID segregation on mechanical properties of weld metal has not been discussed. Haslberger et al[9] suggested that the impact toughness fluctuations and the hardness inhomogeneity of a V-alloyed weld metal were related to the inter-dendritic segregation of alloying elements, but no further work has been carried out to clarify the reasons. Sun et al[14] studied a Fe-Ni-Cr-Mo weld metal with different V content under post-weld heat treatment condition and found that the nanoscale carbides were mainly distributed at ID regions, while large carbides nucleated only at DC regions, causing by the ID segregation of V and Mo.

Different from the work mentioned above, in this study, we focused on the effect of inter-dendritic segregation on microstructure evolution and mechanical properties of TIG-welded part of the component in a welded rotor mock. Thermo-kinetic simulations were carried out to predict the extent of ID segregation at original columnar grain zone during solidification. High-resolution techniques of TEM and Focused Ion Beam (FIB) were used to characterize the microstructures at ID regions and DC regions. The orientation relationship between lath martensite and retained austenite was analyzed, and the difference in chemical compositions between retained austenite and lath martensite was studied by scanning transmission electron microscopy (STEM). The relationship between morphology and nucleation site of retained austenite was studied by T-EBSD. Finally, the effect of ID segregation on the mechanical properties was studied by nano-indentation and impact toughness tests.

II. EXPERIMENTAL MATERIALS AND METHODS

A. *Materials and Welding*

A 1:1 welded rotor mock was fabricated by multi-layer and multi-pass welding technique. The external diameter and the internal diameter of the mock are 840 and 460 mm, respectively, as shown in Figure 1(a). Narrow gap tungsten inert-gas welding (NG-TIG) was used for the backing part and narrow gap submerged arc welding (NG-SAW) for the filling part of this girth weld. The depth and width of the welds are 190 and 20 mm, respectively. The depth of NG-TIG weld metal is 55 mm, and the rest part is NG-SAW weld metal, as shown in Figure 1(b). The NG-TIG weld metal was studied in this paper. The welding direction (WD), build-up direction (BD) and transverse direction (TD) of welded rotor mock are also shown in Figures 1(a) and (b). The chemical compositions of the base metals (BM) and the fusion zone (FZ) obtained by Optical Emission Spectrometer (OES) are listed in Table I and welding parameters are listed in Table II.

B. *Microstructure Observation*

A sample with a size of 15 mm × 10 mm × 5 mm (corresponding to the welding direction) was cut and the surface determined by the directions TD and BD was mechanically polished for metallographic observation, as shown in Figure 1(b). The sample was etched for 10 seconds by 3 pct nital solution, and then characterized by CX14 Optical Microscope (OM) and LYRA3 Scanning Electron Microscope (SEM). The specimens for EBSD analysis were electropolished. The electro-polishing was conducted in an electrolyte solution composed of 65 mL phosphoric acid, 15 mL sulfuric acid, 12 mL glycerol, 3 mL water and 5 g chromium trioxide at a voltage of 6 V and 75 °C. EBSD examination was performed with a 200 nm step size, and the data were analyzed using TSL-OIM Analysis Software. In order to obtain the compositions distribution characteristics of the columnar grain zone of weld metal, JXA8230 Electro-Probe Microanalyzer (EPMA) was used to carry out quantitative analysis with a step size of 3 μm. Additionally, thin foils containing ID region and DC region were prepared by FIB and examined using FEI G20 TEM and T-EBSD.

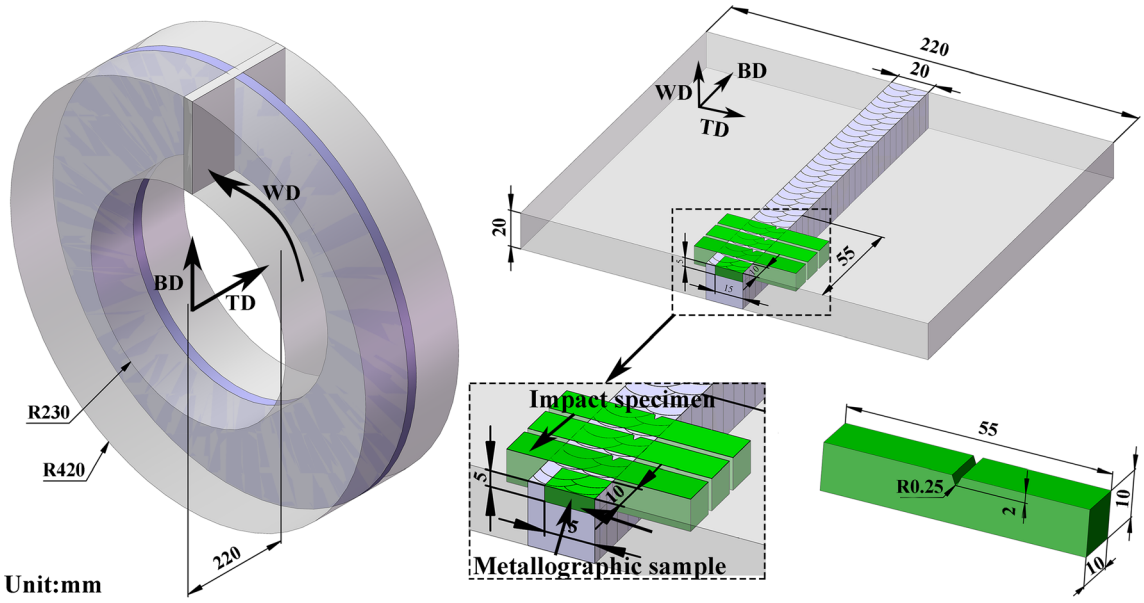

Fig. 1—(*a*) The schematic of the welded rotor mock, (*b*) the position of specimens for impact test and metallographic observation, and (*c*) the size of the impact specimen.

Table I. The Chemical Compositions of Base Metal and Fusion Zone (Wt Pct)

Elements	C	Si	Mn	P	S	Cr	Mo	Ni	V	Cu	Fe
BM	0.25	0.05	0.2	0.004	0.003	2.36	0.76	2.23	0.07	<0.12	Bal.
TIG FZ	0.08	0.61	1.46	0.005	0.004	0.39	0.52	1.55	0.016	0.084	Bal.
SAW FZ	0.06	0.41	1.45	0.006	0.004	0.56	0.49	2.24	0.009	0.055	Bal.

Table II. The Welding Parameters of NG-TIG and NG-SAW

Welding Methods/Welding Parameters	Current (A)	Voltage (V)	Speed (mm/min)	Interpass Temperature (°C)	Gas
NG-TIG	270	11.2	70	200	Ar 99.999 pct
NG-SAW	420	29	420	150	—

C. *Mechanical Tests*

The Charpy V-notch (CVN) impact tests were performed according to ASTM E23 at room temperature. The V-shaped notch was located at 1/4 length of weld metal along transverse direction, and the direction of the notch was parallel to the welding direction to ensure that the crack propagation could pass through the columnar grain zone and reheat grain zone of weld metal alternatively, as shown in Figure 1(b). The dimension of Charpy V-notch impact specimens was 10 × 10 × 55 mm, as shown in Figure 1(c). The impact fracture morphology and crack propagation path were observed by SEM.

In order to characterize the mechanical properties of micro zone in weld metal, nano-indentation tests were carried out on the sample surface using CSM NHT2 nano indenter. The maximum load was 3 mN, the loading/unloading rate was 6 mN/min, the load holding time was 5 seconds, and the indentation interval was 2 μm.

III. RESULTS

A. *Microstructure and Chemical Composition Characterization of Columnar Grain Zone*

Figure 2 shows the microstructure of weld metal in TIG-welded part. The heat affected zone, fusion line and weld metal can be clearly seen in Figure 2(a). In the columnar grain zone, the direction of dendritic growth was different during solidification, as shown in Figure 2(b). The dendrite arm space was about 20 μm,

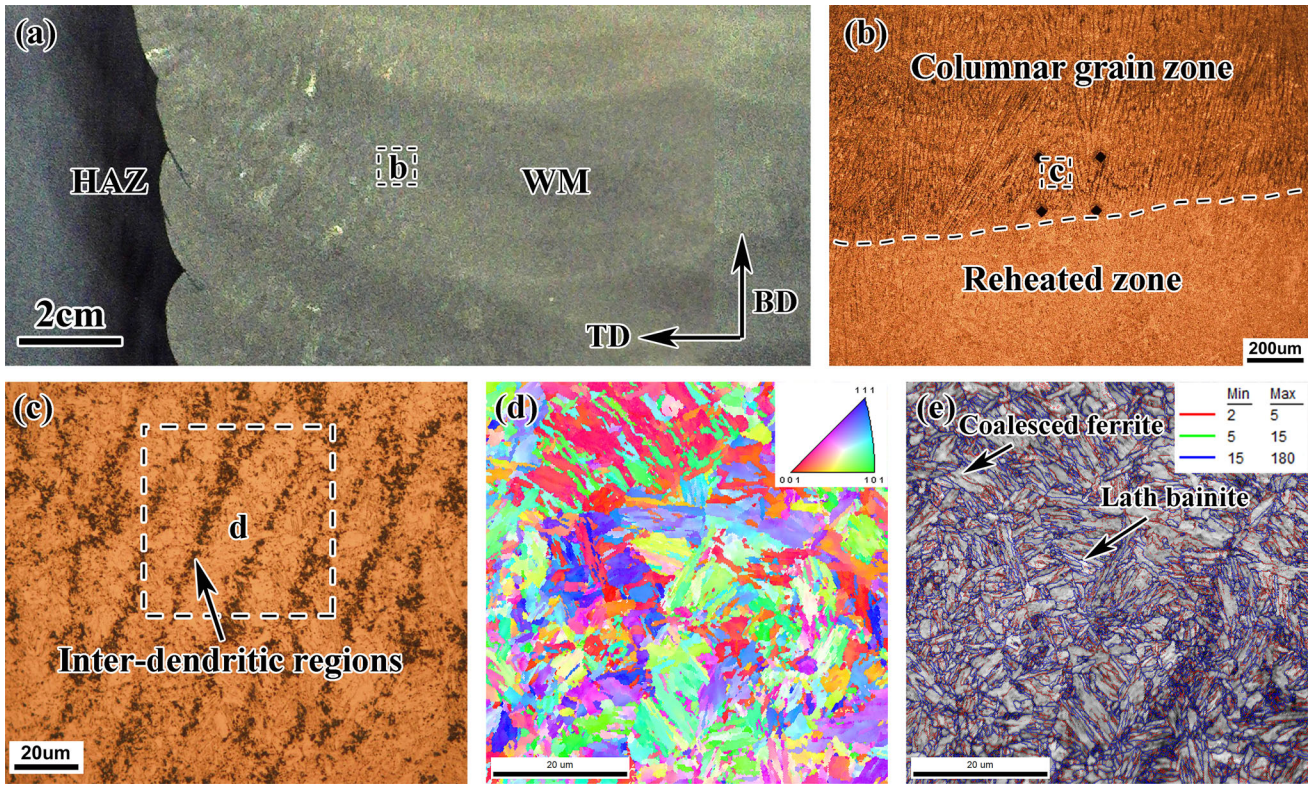

Fig. 2—(*a*) Macrograph of the welded joint, (*b*) detailed micrograph of columnar grain and reheated zone in a, (*c*) magnified microstructure of columnar grain zone in b, (*d*) IPF map of columnar grain zone, and (*e*) image quality (IQ) map + low/high-angle distribution of columnar grain zone.

and the ID regions (dark bands) appeared C enriched due to heavy etching in Figure 2(c). Figures 2(d) and (e) show the Inverse pole figures (IPF) map and image quality (IQ) +low/high-angle grain boundaries distribution map of columnar grain zone. There were many small-angle boundaries (2 deg to 5 deg, red line) and large-angle boundaries (≥ 15 deg, blue line) within DC regions as shown in Figure 2(e), corresponding to a large amount of lath structure and a small amount of blocky structure microstructure, which indicated that the microstructure in DC regions was lath bainite and coalesced ferrite.

Figure 3 shows the SEM micrograph and composition distribution of columnar grain zone. In order to ensure the correspondence between the chemical composition and microstructure along the scan line, indentations microhardness was used to mark the initial point, as shown in Figure 3(a). In Figure 3(b), the inhomogeneous microstructure at ID region was observed with the width of about 5 μm. Composition profiles (EPMA results) of alloy elements across the ID and DC regions in columnar grain zone are shown in Figure 3(c). The nominal composition of Mn and Ni was indicated by the dashed line. The distribution of Mn and Ni elements was inhomogeneous, and mainly enriched at ID regions. However, the distribution of Cr and Si was almost uniform between ID and DC regions. In Figure 3(c), the mean value of Ni content was below the bulk composition and the mean value of Mn content was above the bulk composition. The difference between mean and bulk values might be due to different methods. The mean values of Ni and Mn content in Figure 3(c) were obtained by EPMA, while the bulk compositions were obtained by OES. The area that OES examined was much larger than that EPMA examined. The results obtained by EPMA were more sensitive to the area selected for examination.

B. *Detailed Characterization of ID Region by TEM and T-EBSD*

In our present study, in order to obtain more accurate microstructure information of ID and DC regions, especially the interface between ID and DC regions, the FIB technique was used to accurately obtain the thin foils for TEM analysis. Figure 4(a) shows the SEM morphology of columnar grain zone. The detailed microstructure and location of FIB cutting are shown in Figure 4(b). The thin foil prepared by FIB contained both the ID and DC regions.

Figure 5 shows the results of TEM observation. Figure 5(a) shows the dark field image of the both ID (in the right side) and DC regions. A flexural interface between ID and DC regions can be observed significantly, and this interface was defined as bainite (B)/martensite (M) interface. The microstructure on the right side of Figure 5(a) shows the lath structure feature, and the width of lath structure is about 1 μm. Furthermore, many bright 'particles' (highlight areas) were distributed at the substructure boundaries.

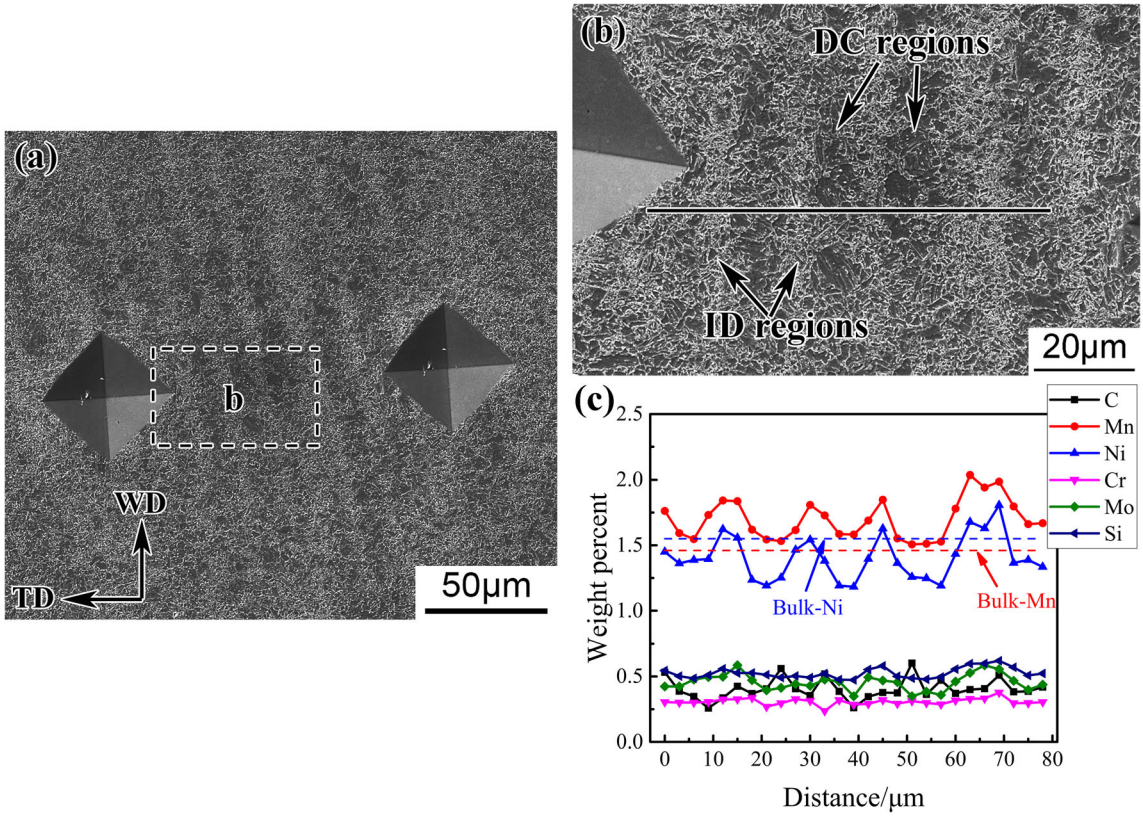

Fig. 3—(*a*) Line scan extends across dendritic structure bounded by microhardness indentations, (*b*) detailed microstructure of ID and DC regions, (*c*) the chemical composition profiles across the ID and DC regions obtained by EPMA along the scanning line in b.

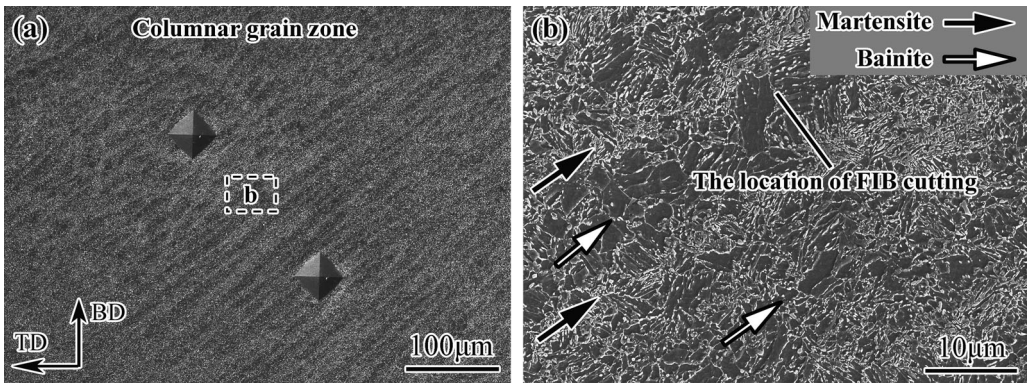

Fig. 4—(*a*) SEM morphology of columnar grain zone, (*b*) detailed microstructure of columnar grain zone, and the location of FIB cutting across dendritic structure.

Figure 5(b) shows the magnified morphology of lath structure, and there were also many 'particles' distributed at substructure boundaries. Figure 5(c) shows the bright field image corresponding to Figure 5(b), and the 'particles' was observed at a higher magnification, as shown in Figure 5(d). Figure 5(e) shows the results of the selected area diffraction (SAD) patterns of 'particles' in Figure 5(d). The 'particle' was confirmed to have face-centered cubic (fcc) structure with the lattice parameter 0.3535 nm. Figure 5(f) shows the result of Energy Disperse Spectroscopy (EDS) analysis of 'particles' in Figure 5(d), and the contents of main alloying elements, Mn and Ni, are higher than the nominal contents. The peak of Cu was obviously higher due to the copper net used for thin foil. Based on the above results of TEM morphology, SAD patterns and EDS analysis, it can be confirmed that the 'particle' was blocky retained austenite. The film-like structure on the top side in Figure 5(a) was also identified as retained austenite by using the same method. In addition, no M_3C carbides can be found at ID region, indicating the microstructure of ID region was composed of untempered martensite and retained austenite.

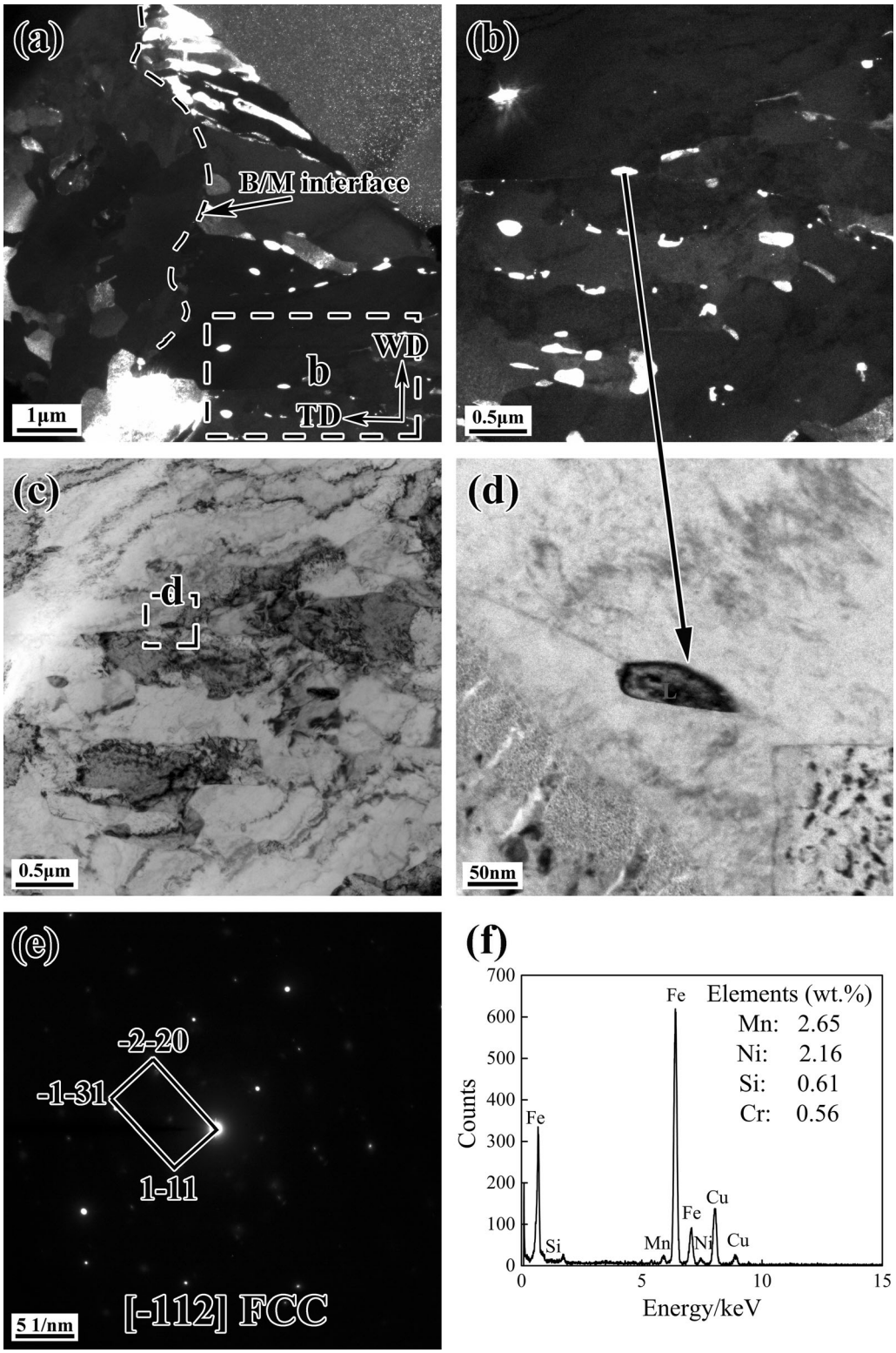

Fig. 5—(*a*) TEM dark field image of both ID and DC regions obtained from thin foil, (*b*) detailed TEM morphology in a, (*c*) TEM bright field image corresponding to b, (*d*) magnified observation of retained austenite in c, (*e*) SAD pattern of retained austenite in d, and (*f*) EDS result of retained austenite in d.

Figure 6(a) shows the TEM bright field image of ID regions and the position of the SAD aperture (indicated by red circle) in both retained austenite and martensite. Figure 6(b) shows the high-angle annular dark field (HAADF) image of film-like retained austenite by STEM. The composition profile obtained by EDS line

scanning showed that the film-like retained austenite was rich in C, Mn and Ni. Figure 6(c) shows the magnified observation of retained austenite in Figure 6(a). Further EDS analysis results revealed that Mn in film-like retained austenite was enriched to 3.05 wt pct, as shown in Figure 6(d). The contents of

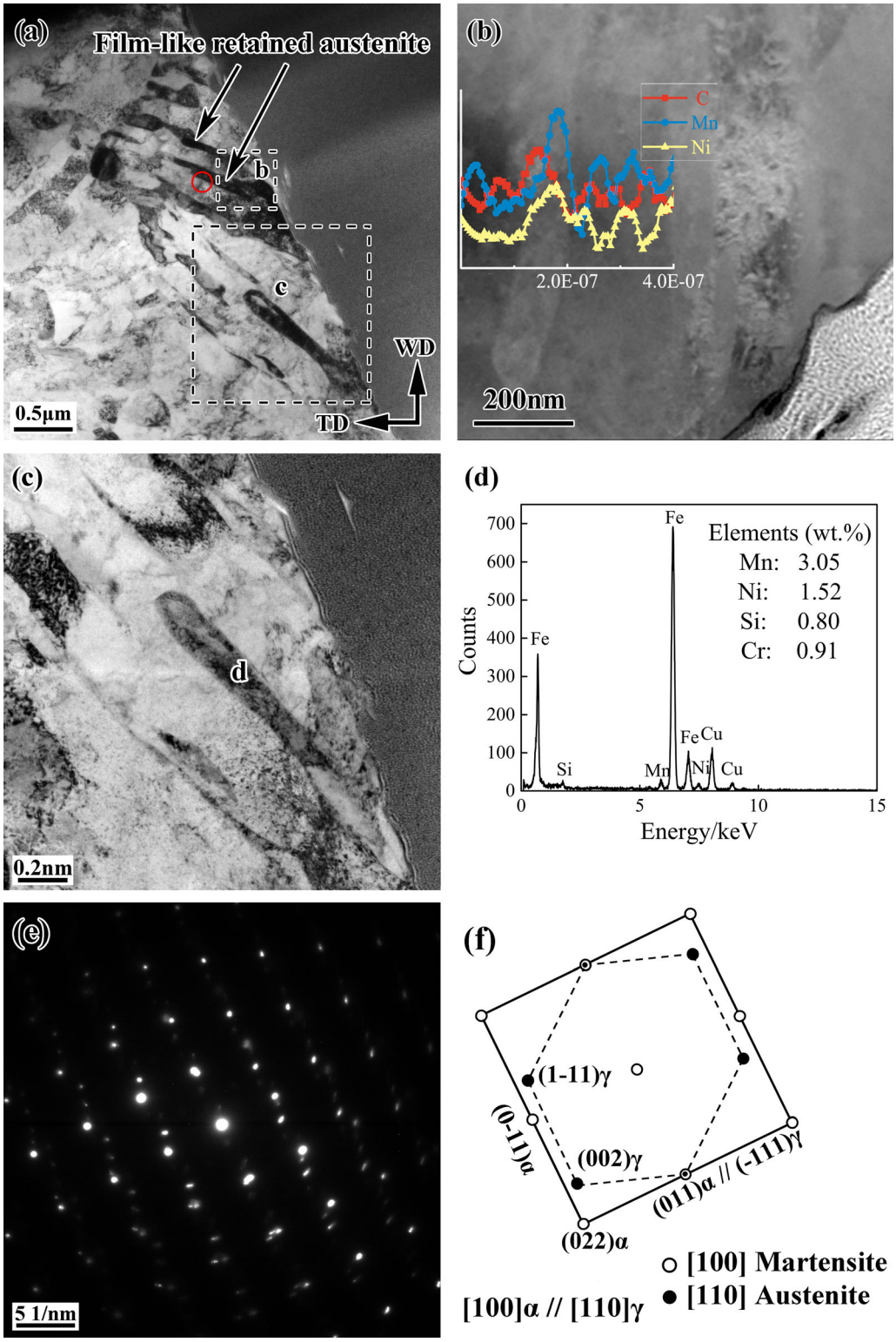

Fig. 6—(*a*) TEM bright field image of ID regions, (*b*) STEM-HAADF micrograph of retained austenite and EDS line-scanning results along the horizontal white line, (*c*) Magnified observation of retained austenite in a, (*d*) EDS result of retained austenite in c, (*e*) SAD pattern of the red circle in a, and (*f*) Corresponding schematic illustration: the solid and blank circles indicate the diffraction spots for fcc-austenite and bcc-martensite, respectively.

Mn in both blocky (2.65 wt pct) and film-like retained austenite were higher than those of the ID regions obtained by EPMA. Xie et al[22] suggested that the stability of austenite depends on chemical composition, size, morphology and surrounding phases. In our work, the width of blocky retained austenite [Figure 5(d)] was about 42.68 nm, and the main alloying element content of Mn and Ni content obtained from TEM-EDS was 2.65 and 2.16 wt pct, respectively. While the width of film-like retained austenite in Figure 6(c) was about 156.77 nm, and the content of Mn and Ni content was 3.05 and 1.52 wt pct, respectively. It was consistent with the Xie's work that the larger austenite needed more austenitizing elements to ensure its stability.

Figure 6(e) shows the SAD pattern obtained from the aperture covering both film-like retained austenite and martensite [Figure 6(a)]. The corresponding schematic illustration is shown in Figure 6(f). Figure 6(f) shows that the orientation relationships are $(011)_\alpha//(-111)_\gamma$ and $[100]_\alpha//[110]_\gamma$, indicating that the orientation relationship between γ and α matrix obeys the Nishiyama-Wasserman (N–W) type of $\{110\}_\alpha//\{111\}_\gamma$ and $<110>_\alpha//<112>_\gamma$.[23] Zhang et al[24] reported that both film-like or acicular and blocky or globular austenite held a near Kurdjumov–Sachs (K–S) orientation relationship with at least one of its surrounding tempered martensite blocks. Different from previous studies, in our study, the film-like austenite formed at martensite lath boundaries has the same orientation with the prior austenite, and has a N–W relationship with its surrounding untempered martensite laths. However, whether a determinate orientation relationship of blocky austenite to the adjacent martensite could not be determined in the present work.

Figure 7 shows the T-EBSD results of ID and DC regions near the B/M interface. As shown in Figure 7(a), the IQ + the low/high-angle grain boundaries distribution maps suggested that the film-like retained austenite distributed at the low-angle boundaries (red lines) in ID region, and the blocky retained austenite distributed at the high-angle boundaries (blue lines) at ID region. The IPF map in Figure 7(b) indicates that the orientation of lath martensite on both sides of the film-like retained austenite was almost the same, while martensite distributed around the blocky retained austenite had a larger misorientation. Nakada, Wei and Zhang *et al.* reported that the morphology of retained/reversed austenite depended on their nucleation sites.[25–27] Matsuda and Hara *et al.* indicated that the film-like or acicular austenite was nucleated at martensite packet, block or lath boundaries,[28] while blocky or globular austenite was nucleated at prior grain boundaries as well as martensite packet and block boundaries.[29] In our present study, the film-like retained austenite distributed at martensite lath boundaries (low-angle boundaries), and the blocky retained austenite distributed at martensite block or packet boundaries (high-angle boundaries). It is noteworthy that the B/M interface was identified as high-angle grain boundaries in Figure 7(b), along which the morphology of retained austenite was blocky, consistent with the distribution characteristic mentioned above.

C. *Mechanical Properties*

In order to reveal the mechanical difference between ID and DC regions, nano-indentation test was carried out on the columnar grain zone. Figure 8 shows the nano-hardness distribution of the columnar grain zone containing ID and DC regions. From the hardness profile, it is easy to find that the hardness of ID and DC regions was very close to each other. The average hardness of all the DC regions was 4.11 GPa and that of the ID regions was 4.22 GPa. The nano-hardness of ID regions was slightly higher than that of DC region despite obviously different microstructures in the two regions. It is generally assumed that martensite is harder than bainite and ferrite, and carbon content is the key factor influencing martensite hardness.[30] While in the present study, a great part of carbon segregated in the retained austenite, resulting in relatively low carbon content in the martensite, and that might be the reason for the slight difference in hardness between ID and DC regions.

The impact absorbed energy of the NG-TIG weld metal at room temperature was 180 ± 14 J, and the fracture morphology is shown in Figure 9. Figure 9(a) shows the macro-fracture morphology. The whole fracture presented ductility fracture with obvious plastic deformation, and the shear lip area on both sides of the fracture was larger, which matched with the higher impact energy. The magnified observation of the fracture shown that the fracture presented a columnar morphology, and the size was equivalent to the width of the dendrite arm space, as shown in Figure 9(b). The tear ridges were observed at the dendrite arms, and the interior of the dendrite was relatively flat featuring small cleavage plane, indicating the higher crack propagation resistance at ID region, as shown in Figure 9(c).

The crack propagation path was observed by SEM, as shown in Figures 9(d) and (e). In Figure 9(d), no secondary cracks were found in the area near the crack propagation path, and large-angle deflections during the crack propagation were observed. The magnified observation of the crack propagation path in Figure 9(e) shows that when the crack propagated at DC region and encountered at ID region, it deflected immediately by nearly 90°. Then the crack propagated a very short distance within ID region and deflected again back to another DC region, forming a staircase-like crack propagation path. The staircase-like crack propagation path increased the total length of crack, as a consequence, the crack propagation rate was lower and more energy was consumed.[31] Nakada *et al.*[32] summarized the several mechanisms of the retained austenite increasing the crack propagation resistance, (1) crack branching, (2) crack blunting, and (3) the effect of transformation induced plasticity (TRIP). We considered that the effect of retained austenite in our work resulting in a decrease in stress concentration, and an extra stress was needed for crack propagation, which was consistent with the effect of crack blunting. Except for the effect of retained austenite on hinder the crack propagation, the deflection of crack propagation caused by the interface between ID and DC region is another

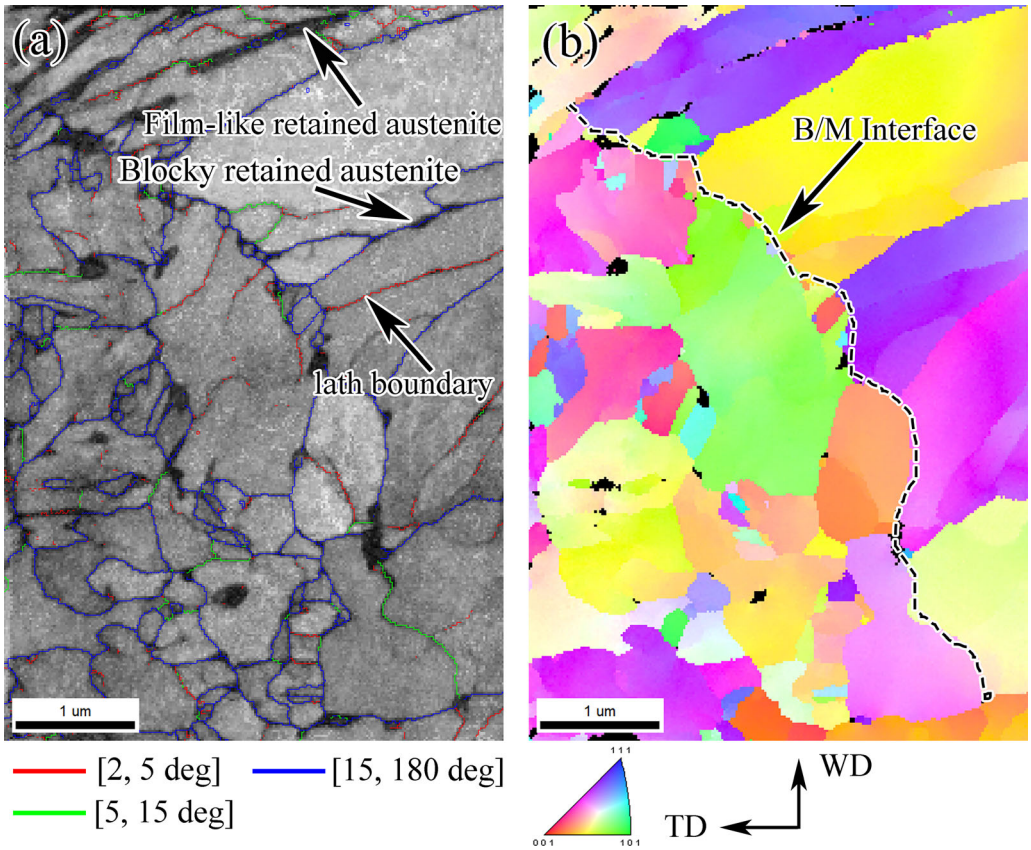

Fig. 7—(*a*) IQ + low/high-angle distribution maps of DC and ID regions obtained by T-EBSD, (*b*) IPF maps of DC and ID regions.

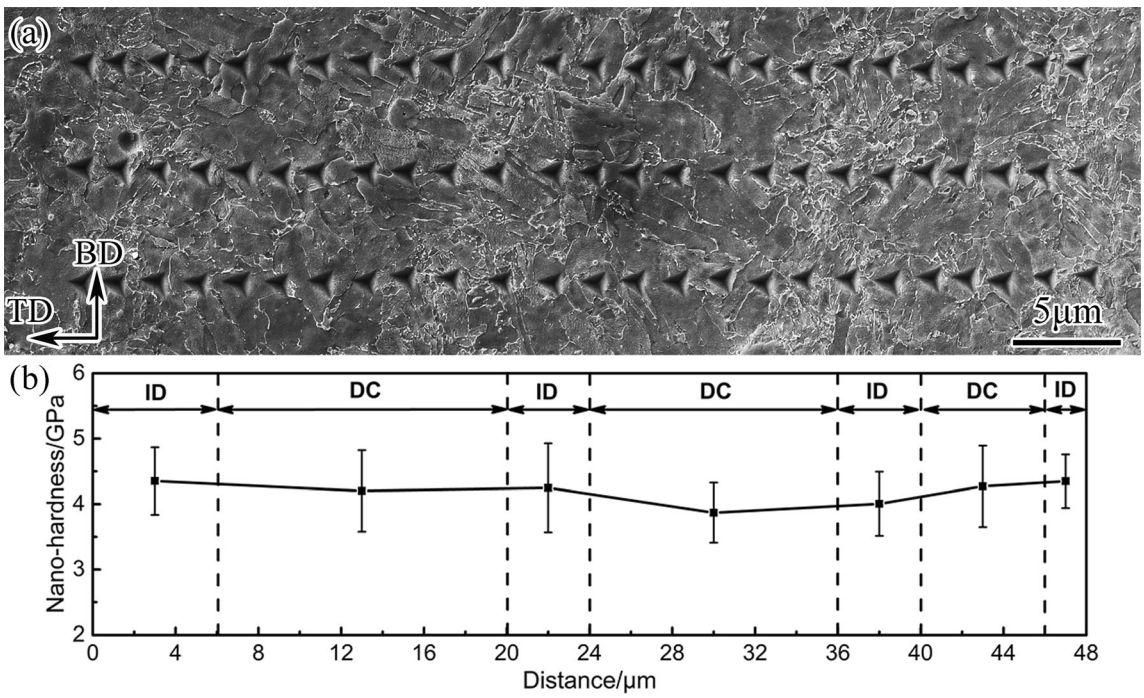

Fig. 8—(*a*) SEM morphology for nano-indentation test, (*b*) the distribution of nano-hardness of columnar grain zone containing ID and DC regions.

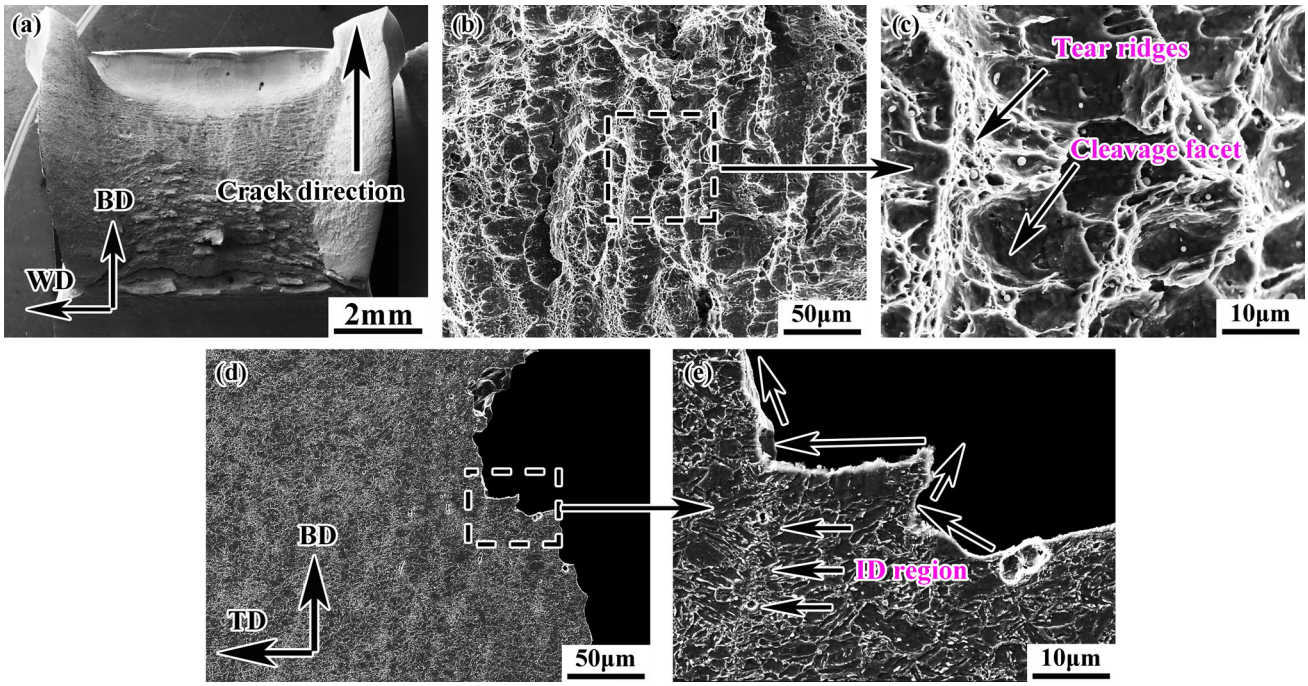

Fig. 9—(*a*) Macroscopic fractography of weld metal, (*b*) low magnification fracture morphology features, (*c*) magnified observation of the area in b, (*d*) crack propagation path, and (*e*) magnified observation of the area in d.

factor contributing to the higher impact toughness of weld metal.

IV. DISCUSSION

In order to better understand the diffusion behavior of alloy elements during welding solidification, Scheil solidification simulation was performed using Thermo-Calc software and TCFE7 thermodynamic database. The nominal composition of fusion zone was used as the composition of the liquid phase for Scheil solidification simulation. Figure 10 shows the results of Scheil solidification simulation. Figure 10(a) shows the dependence of solid phase fraction on temperature. When the temperature reaches liquidus temperature (1509 °C), the solidification begins, and δ-ferrite precipitate firstly. When the temperature reaches 1484 °C, γ-austenite precipitates from the liquid in the Scheil mode, and the mass fraction of the solid phase is 0.7. With the decrease of temperature, the solidification rate decreased. When the mass fraction of solid phases reaches 99 pct, the solidification is considered to be complete, and the calculated solidus temperature is 1215 °C. Figure 10(b) shows the weight percent of main alloying element C, Mn and Ni in δ-ferrite and γ-austenite. With the increase of mass fraction of solid phases, the content of C, Mn and Ni in solid phases (δ and γ) increases. It is obvious that the increase rate of C, Mn and Ni contents in γ-austenite is higher than that in δ-ferrite. The contents of those alloying elements fluctuates simultaneously when the austenite precipitates. Table III shows the nominal composition of fusion zone and detailed chemical composition at ID and DC regions obtained by EPMA and Scheil solidification simulation, respectively. The EPMA experiment results in Table III are taken from the maximum value at ID region and the minimum value at DC region of each alloying element in Figure 3(c). The results of Scheil solidification simulation show that the contents of main alloying elements at ID region is higher than that at DC region and the nominal composition of fusion zone. The distribution characteristic of alloying elements at ID and DC regions predicted by Scheil solidification simulation is similar to EPMA experimental results, but the specific contents of alloying elements at ID and DC regions is different. The calculated results only represent the composition at ID and DC when the solidification is complete due to the redistribution of composition during the subsequent phase transformation. This is a possible reason for the difference between the above calculated and experimental results.

The heterogeneous distribution of alloying elements within 10 μm (from ID to DC region) induces the different ferritic products formed during further cooling. In order to illustrate the relationship between solidification segregation and heterogeneous microstructure, JMatPro software was used to construct the continuous cooling transformation (CCT) diagram. The chemical composition of ID and DC regions taken from Scheil solidification simulation results were used to describe CCT diagram, respectively. The cooling rate was set as 20 °C/s to simulate welding cooling rate. Figure 11(a) shows the CCT curves of ID and DC regions, and Figure 11(b) shows the schematic of microstructure evolution. When the temperature is higher, the microstructure of dendrite is full austenite, and the content of alloying elements in austenite increases

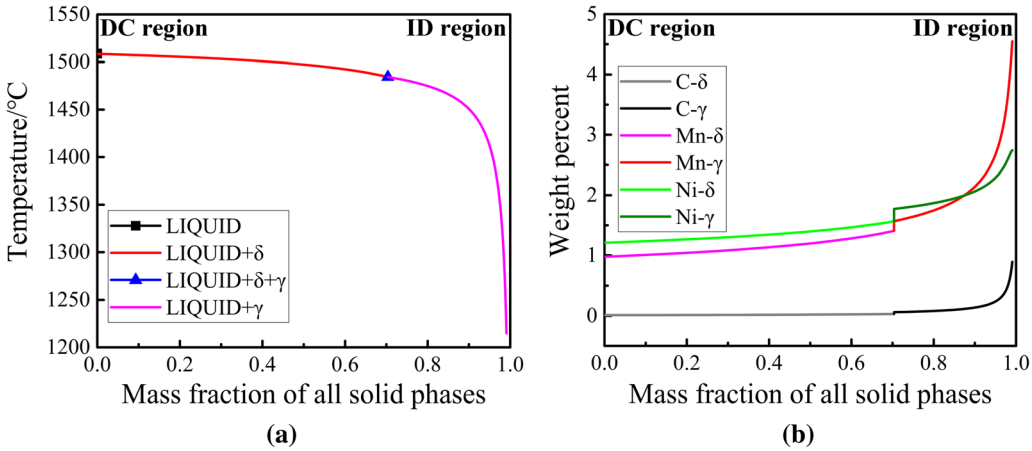

Fig. 10—(*a*) The relationship between temperature and solid phase fraction of Scheil solidification simulation, (*b*) the chemical composition in solid phases during solidification.

Table III. The Nominal Composition of Fusion Zone and the Chemical Composition of the ID and DC Obtained by EPMA and Scheil Solidification Simulation, Respectively (Wt Pct)

	C	Si	Mn	Cr	Mo	Ni	V	Cu
Nominal	0.08	0.61	1.46	0.39	0.52	1.55	0.016	0.084
EPMA								
ID	0.60	0.62	2.04	0.38	0.59	1.81	—	—
DC	0.26	0.47	1.51	0.24	0.35	1.18	—	—
Scheil								
ID	0.89	2.55	4.55	0.44	1.28	2.74	0.01	0.11
DC	0.01	0.39	0.98	0.36	0.40	1.21	0.01	0.07

gradually from DC region to ID region, as shown in Figure 11(b). With the decrease of temperature, the cooling curve (green solid curve) encounters F_s curve (black dashed curve), austenite at DC regions begins to transform into ferrite partially. Subsequently, the cooling curve encounters B_s curve (red dashed curve) and the remained austenite transformed into bainite till room temperature. As a result, the microstructure of DC regions is a mixture of ferrite and bainite, as shown in Stage 2, Figure 11(b). The austenite at DC regions transforms into ferrite and bainite at a higher temperature due to its poor stability and lower hardenability. While for ID regions, the enrichment of alloying elements makes the CCT curve shift to the right side and improves the stability of austenite. The austenite at ID regions occupies higher hardenability and stability than that at DC regions, which means that it is easier for ID regions to transform to martensite at a lower M_s temperature. Besides, the enrichment of alloying elements makes the M_f temperature lower than ambient temperature, the martensitic transformation cannot be carried out completely, and part of austenite will be retained. Finally, the microstructure of columnar grain zone at the ambient temperature is composed of ferrite + bainite (DC region) and martensite + retained austenite (ID region). The enrichment of alloying elements caused by solidification segregation not only changes the austenite decomposing temperature at ID and DC regions, but also renders austenite at ID and DC regions transforming into different products.

V. CONCLUSION

The effect of welding solidification segregation on the microstructure and mechanical properties of a rotor weld metal was investigated. The major conclusions of this work can be summarized as follows:

1. The solute elements (k_{ele}<1), such as Mn and Ni, segregated toward ID region during welding solidification, and the degree of Mn and Ni enrichment was higher.
2. The segregation of alloying elements at ID region improved the stability of austenite and suppressed austenite to bainite transformation, making the untempered martensite and retained austenite formed at ID region.
3. The morphology of retained austenite within ID region depended on the nucleation sites. The film-like retained austenite distributed at low-angle martensite laths boundaries and held N–W orientation relationship with surrounding matrix, while blocky retained austenite distributed at high-angle boundaries and the B/M interface. Both film-like and blocky retained austenite had a higher content of alloying elements than surrounding matrix.
4. The ID region had a slightly higher nano-hardness than the DC region, which was attributed to the finer size and higher dislocation density of martensite laths.

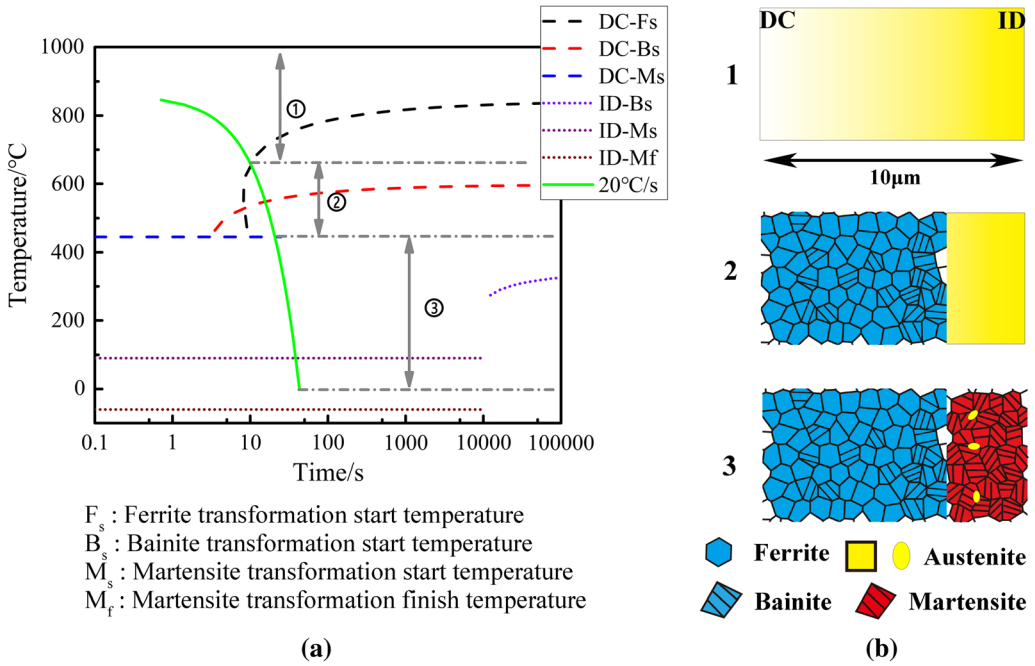

Fig. 11—(*a*) CCT diagram of ID and DC region, (*b*) the schematic of the microstructure evolution.

5. The mixture microstructure of untempered martensite and retained austenite at ID region had a great effect on hindering the crack propagation, making crack deflection, and improving the impact toughness of the weld metal.

ACKNOWLEDGMENTS

This work was supported by National Key R&D Program of China (Nos. 2020YFA0714900), the Defense Industrial Technology Development Program (JCKY2020110B007), and National Natural Science Foundation of China (No. 52031003).

CONFLICT OF INTEREST

The authors declare that they have no known competing financial interests or personal relationships that could have appeared to influence the work reported in this paper.

REFERENCES

1. P. Liu, F. Lu, X. Liu, H. Ji, and Y. Gao: *J. Alloy Compd.*, 2014, vol. 584, pp. 430–37.
2. R. Chen, J. Gu, L. Han, and J. Pan: *Mater. Sci. Technol.*, 2012, vol. 28, pp. 773–77.
3. Z. Wang, X. Wang, Y. Nan, C. Shang, X. Wang, K. Liu, and B. Chen: *Mater. Charact.*, 2018, vol. 138, pp. 67–77.
4. T. Zhang, Z. Li, F. Young, H.J. Kim, H. Li, H. Jing, and W. Tillmann: *ISIJ Int.*, 2014, vol. 54, pp. 1472–84.
5. X. Qi, H. Di, Q. Sun, X. Wang, X. Chen, Y. Gao, and Z. Liu: *J. Mater. Eng. Perform.*, 2019, vol. 28, pp. 7006–15.
6. P. Zhou, B. Wang, L. Wang, Y. Hu, and L. Zhou: *Mater. Sci. Eng. A*, 2018, vol. 722, pp. 112–21.
7. Y. Li, Z. Cai, K. Li, J. Pan, X. Liu, L. Sun, and P. Wang: *J. Mater. Res.*, 2018, vol. 33, pp. 923–34.
8. X.L. Wang, Y.R. Nan, Z.J. Xie, Y.T. Tsai, J.R. Yang, and C.J. Shang: *Mater. Sci. Eng. A*, 2017, vol. 702, pp. 196–205.
9. P. Haslberger, W. Ernst, C. Schneider, S. Holly, and R. Schnitzer: *Weld. World*, 2018, vol. 62, pp. 1153–58.
10. M.A. Quintana, S. Babu, J. Major, C. Dallam, M. James: International Pipeline Conference, 2010, pp. 599-608.
11. O. Grong and D.K. Matlock: *Int. Met. Rev.*, 1986, vol. 31, pp. 27–48.
12. Z. Zhang and R. Farrar: *J. Mater. Sci.*, 1995, vol. 30, pp. 5581–88.
13. Z. Zhang and R. Farrar: *Weld J.*, 1997, vol. 76, p. 183.
14. J. Sun and S. Lu: *Scr. Mater.*, 2020, vol. 186, pp. 174–79.
15. P. Haslberger, S. Holly, W. Ernst, and R. Schnitzer: *Weld. World*, 2018, vol. 62, pp. 713–19.
16. G. Krauss: *Metall. Mater. Trans. B*, 2003, vol. 34B, pp. 781–92.
17. M. Perricone and J. Dupont: *Metall. Mater. Trans. A*, 2006, vol. 37A, pp. 1267–80.
18. G. Powell and G. Herfurth: *Metall. Mater. Trans. A*, 1998, vol. 29A, pp. 2775–84.
19. E. Keehan, L. Karlsson, and H.O. Andrén: *Sci. Technol. Weld. Jt.*, 2013, vol. 11, pp. 1–8.
20. E. Keehan, L. Karlsson, H.O. Andrén, and H.K.D.H. Bhadeshia: *Sci. Technol. Weld. Jt.*, 2013, vol. 11, pp. 9–18.
21. E. Keehan, L. Karlsson, H.O. Andrén, and H.K.D.H. Bhadeshia: *Sci. Technol. Weld Jt.*, 2013, vol. 11, pp. 19–24.
22. Z. Xie, G. Han, Y. Yu, C. Shang, and R. Misra: *Mater Charact.*, 2019, vol. 153, pp. 208–14.
23. H. Beladi, V. Tari, I.B. Timokhina, P. Cizek, G.S. Rohrer, A.D. Rollett, and P.D. Hodgson: *Acta Mater.*, 2017, vol. 127, pp. 426–37.
24. X. Zhang, G. Miyamoto, Y. Toji, S. Nambu, T. Koseki, and T. Furuhara: *Acta Mater.*, 2018, vol. 144, pp. 601–12.
25. N. Nakada, T. Tsuchiyama, S. Takaki, and N. Miyano: *ISIJ Int.*, 2011, vol. 51, pp. 299–304.
26. R. Wei, M. Enomoto, R. Hadian, H. Zurob, and G. Purdy: *Acta Mater.*, 2013, vol. 61, pp. 697–707.
27. X. Zhang, G. Miyamoto, T. Kaneshita, Y. Yoshida, Y. Toji, and T. Furuhara: *Acta Mater.*, 2018, vol. 154, pp. 1–13.
28. S. Matsuda and Y. Okamura: *Trans. Iron Steel Inst. Jpn.*, 1974, vol. 14, pp. 363–68.

29. T. Hara, N. Maruyama, Y. Shinohara, H. Asahi, G. Shigesato, M. Sugiyama, and T. Koseki: *ISIJ Int*., 2009, vol. 49, pp. 1792–800.
30. J.P. Galler, J.N. DuPont, S.S. Babu, and M. Subramanian: *Metall. Mater. Trans. A*, 2019, vol. 50A, pp. 2201–17.
31. G. Mao, C. Cayron, R. Cao, R. Logé, and J. Chen: *Mater Charact*., 2018, vol. 145, pp. 516–26.
32. B.N. Rao and G. Thomas: *Metall. Trans. A*, 1980, vol. 11, pp. 441–57.